Effect of Grade on Thermal–Mechanical Behavior of Steel During Initial Solidification

MATTHEW L.S. ZAPPULLA, LANCE C. HIBBELER, and BRIAN G. THOMAS

Thermal–mechanical analysis of solidification is important to understand crack formation, shape problems, and other aspects of casting processes. This work investigates the effect of grade on thermal–mechanical behavior during initial solidification of steels during continuous casting of a wide strand. The employed finite element model includes non-linear temperature-, phase-, and carbon content-dependent elastic–viscoplastic constitutive equations. The model is verified using an analytical solution, and a mesh convergence study is performed. Four steel grades are simulated for 30 seconds of casting without friction: ultra-low-carbon, low-carbon, peritectic, and high-carbon steel. All grades show the same general behavior. Initially, rapid cooling causes tensile stress and inelastic strain near the surface of the shell, with slight complementary compression beneath the surface, especially with lower carbon content. As the cooling rate decreases with time, the surface quickly reverses into compression, with a tensile region developing toward the solidification front. Higher stress and inelastic strain are generated in the high-carbon steel, because it contains more high-strength austenite. Stress in the δ-ferrite phase near the solidification front is always very small, owing to the low strength of this phase. This modeling methodology is a step toward designing better mold taper profiles for continuous casting of different steels.

DOI: 10.1007/s11661-017-4112-z

I. INTRODUCTION

THE surface quality of cast metal products depends significantly on initial solidification behavior. In casting processes, such as continuous casting, die casting, and ingot casting, defects such as cracks, segregation, porosity, and microstructural or grain defects that appear in the newly solidified shell may evolve and lead to problems in the final product, even after many subsequent processing steps. Thermal stress generation is an important aspect of many of these defects.

Steel composition strongly affects the surface quality of continuously cast steels, especially for grades involving the peritectic transformation. In addition, each steel grade has slightly different shell growth, shrinkage, and thermal–mechanical characteristics. Fundamental understanding of these phenomena is especially required when developing and solving problems in new steel grades, such as advanced high-strength steels (AHSS). The extreme environment of steel casting processes makes experimentation difficult. Thus, modeling is an important tool in the development of this understanding.

The thermal and mechanical behavior of the solidifying shell within a mold is explored in this work using a computational model. Four steel grades are studied to explore the typical behavior of different types of phase transformation histories in the iron-rich side of the Fe-Fe_3C phase diagram.

II. PREVIOUS WORK

The modeling of solidification phenomena has been a very active area of research. Some reviews of the previous literature have focused on modeling of grain structures and defects,[1] macrosegregation,[2] microstructure development,[3] and the effects of alloying elements.[4] Relatively fewer models have analyzed stress and deformation during solidification.

Small differences in steel composition can greatly change evolution of the phase fractions during solidification,[5, 6] and consequent changes in the material properties and behaviors. Specifically, ultra-low-carbon steels and peritectic steels experience much greater mechanical deformation during solidification than do low- and medium-carbon steels, which consequently causes higher surface roughness, lower and less uniform heat transfer,[7] and greater crack susceptibility.[8–10] Identifying phase fraction histories is a useful step in

MATTHEW L.S. ZAPPULLA is with the Department of Mechanical Science and Engineering, University of Illinois at Urbana-Champaign, 1206 West Green Street, Urbana, Illinois, 61801. LANCE C. HIBBELER is with Intel Corporation, Hillsboro, Oregon, 97124. BRIAN G. THOMAS is with the Department of Mechanical Engineering, Colorado School of Mines, 1610 Illinois Street, Golden, Colorado, 80401, and also with the University of Illinois at Urbana-Champaign. Contact e-mail: bgthomas@mines.edu

Manuscript submitted September 18, 2016.
Article published online May 23, 2017

predicting these phenomena. Tools to study the equilibrium phases of steels have used experimental methods involving slow cooling rates, such as differential scanning calorimetry,[11,12] as well as steel composition-dependent phase diagrams,[13,14] and applying free-energy-based models, such as ThermoCalc[15] and FactSage.[16] Some tools, such as IDS,[17] also model species diffusion to incorporate non-equilibrium kinetic effects in finding the phase fractions.

Steel properties at high temperature are difficult to measure; only a few papers have measured thermal properties[18,19] or conducted mechanical testing in the appropriate regime of low strain (<2 pct), and low strain rates (10^{-5} to 10^{-2} 1/s), which include tensile tests on austenite and ferrite[20,21] and creep tests above 1073 K (800 °C).[22]

Previous macroscale thermal–mechanical modeling work[23–35] has been conducted using temperature-dependent constitutive and material properties including studies for billets,[27–32] slabs,[29,33,36] and other work toward better taper prediction.[25–27,29,32–34]

Other models have used phase field modeling which include studies on hot tear sensitivity[6,37] and microstructure evolution.[38,39] Only a few previous models have investigated the effect of steel grade on initial solidification, such as the deformed shape of solidifying droplets[40] or continuously-cast shells.[24]

The current work models the macroscale thermal–mechanical behavior during the initial solidification of a steel casting process; it presents verification using an analytical solution, and then applies the model to explore the fundamental differences between steel grades, in the context of a typical continuous steel casting process.

III. HEAT FLUX

In the continuous casting process, the instantaneous rate of heat leaving the surface of the solidifying steel shell (heat flux), $\dot{q}_{\text{Inst}}$ (MW/m^2) can be estimated as a function of time down the mold, t, by thermocouples embedded in the mold wall. In addition, the average heat flux leaving the mold $\bar{\dot{q}}_{\text{Avg}}$ (MW/m^2) can be found by measuring the increase in temperature and flow rate of the cooling water, and knowing the surface area of the mold in contact with the steel. This average can be converted to the total heat removed, $\bar{Q}_{\text{Tot}}$ (MJ/m^2), during the "dwell time," t_{dwell}, spent by the steel in the mold:

$$\bar{Q}_{\text{Tot}}(\text{MJ/m}^2) = \bar{\dot{q}}_{Avg}(\text{MW/m}^2)t_{\text{dwell}}\,; \quad t_{\text{dwell}} = z_{\text{dwell}}/V_{\text{c}} \qquad [1]$$

where z_{dwell} is the working mold length, and V_{c} is the casting speed, assumed to be constant. Measurements of total mold heat removal, $\bar{Q}_{\text{Tot}}$, from the previous work[28,30,41–46] are plotted *vs* dwell time in Figure 1.

It is convenient to express Q_{Tot}in the following form, with time down the mold:

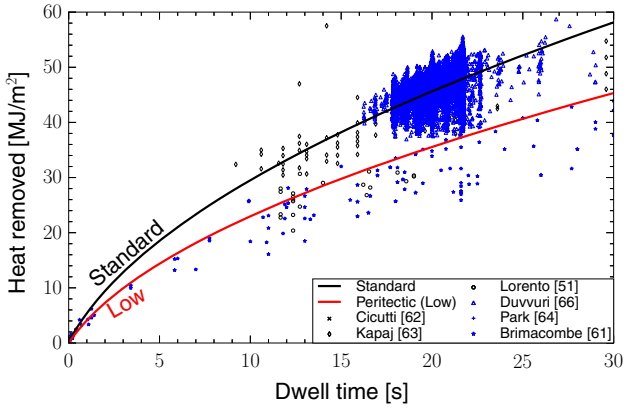

Fig. 1—Measured heat removed and fitted curves.

$$Q_{\text{Tot}} = -ab^n + a(t+b)^n \qquad [2]$$

The time average heat flux in the mold then is given as follows:

$$\bar{\dot{q}}_{\text{Avg}} = \frac{Q_{\text{tot}}(t_{\text{dwell}})}{t_{\text{dwell}}} = \bar{\dot{q}}_0 + \frac{a}{t_{\text{dwell}}}(t_{\text{dwell}}+b)^n \qquad [3]$$

where $\bar{\dot{q}}_0 = -ab^n/t_{\text{dwell}}$. If $b = 0$, Eq. [3] simplifies to

$$\bar{\dot{q}}_{\text{Avg}} = \bar{\dot{q}}_0 + a(t_{\text{dwell}})^{n-1}. \qquad [4]$$

The coefficients for the average heat flux profiles in previous measurements are given in Table I, according to this equation form. The corresponding instantaneous heat flux profile down the mold is found by differentiating Eq. [2]:

$$\dot{q}_{\text{Inst}} = \frac{\text{d}}{\text{d}t}Q_{\text{Tot}} = n \times a(t+b)^{n-1}. \qquad [5]$$

By including non-zero b in Eq. [5], this form has a time-shift that avoids the unrealistic high instantaneous heat flux that is otherwise produced at small times. Thus, the equation form with non-zero b adopted here has the advantage of capturing the approximately linear drop in instantaneous heat flux observed at short times (<1 second) in strip casting processes.[30]

In this work, two different profiles of heat flux (HF) down the mold are used to simulate typical casting conditions, by fitting measurements for "standard" and "low" heat flux conditions to the above equation forms. The total heat removed using these two profiles is given by Eq. [2], and included in Figure 1. Coefficients for these two profiles are included in Table I for the time average and instantaneous forms, given by Eqs. [3] and [5], respectively.

The Standard-HF curve was found by fitting all of the data points in Figure 1 and the Low-HF curve was generated by excluding the higher HF data of Duvvuri *et al.*[46] The Low-HF curve is used for peritectic steels,

Table I. Heat Flux Profile Coefficients

Profile	q_0	a	b	n
Wolf (slag)[45]	—	7.3	—	0.5
Wolf (oil)[45]	—	9.5	—	0.5
Li (Billet)[30]	—	9.57	—	0.496
Li (Slab)[30]	—	4.05	—	0.67
Lorento[28]	—	5.88	—	0.5
Brimacombe[41]	2.68	-0.22	—	0.5
This work (Standard)	—	12.72	1.032	0.5
This work (Low)	—	9.92	1	0.5

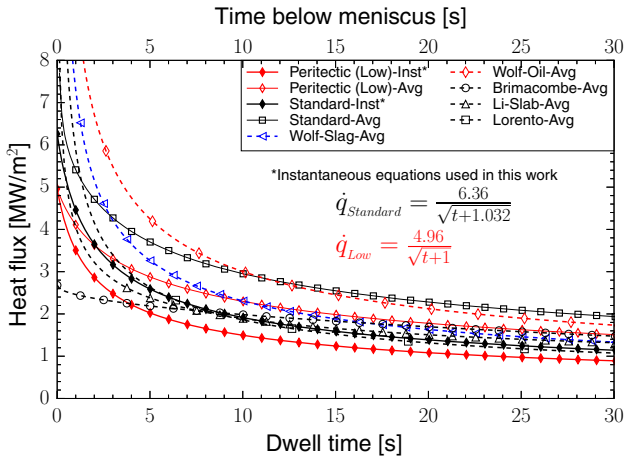

Fig. 2—Instantaneous and average heat flux curves.

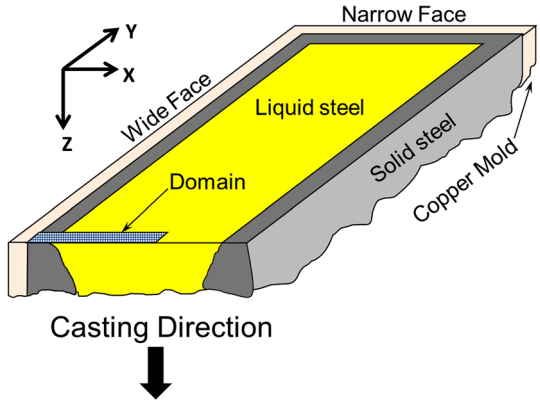

Fig. 3—Initial solidification of a continuous cast slab (cutaway) showing model domain.

which have lower heat flux, owing to their deeper oscillation marks, surface depressions,[47] and usually higher slag crystallization temperatures.[48] Peritectic steels are difficult to cast, due to the mechanical behavior during the peritectic transformation[8,11]; lowering heat removal is one method to lessen castability problems such as longitudinal cracks and depressions.[49]

Figure 2 compares average heat flux formulas from previous literature with those generated for the current work. The standard and low average heat flux curves are plotted using solid lines in black and red, respectively; the corresponding instantaneous heat flux curves are also included, shown with filled diamonds. Note that at any given time down the mold, the instantaneous heat flux is always significantly less than that on the time-average curve, at that dwell time. This difference is a natural consequence of a function that decreases with time.

IV. MODEL DESCRIPTION

This section describes the computational model used in this work, including the domain, heat transfer model, stress model, steel grades studied, and solution details. The solidifying steel is envisioned here as a thin plate constrained against bending. In continuous casting, the shell solidifying in the mold is pushed against the mold hot face by ferrostatic pressure, so this domain represents a typical vertical section through the wide faces of a slab caster, away from the corner region. With perfect contact against the mold wall and uniform solidification, the domain is simply a thin strip "drilled" through the shell thickness, as shown in Figure 3.

The model uses a Lagrangian formulation that follows a slice of material moving down through the mold at the casting speed. This is reasonable for continuous casting of steel, because the advection of heat dominates over the axial heat conduction,[50] which is demonstrated by the large Péclet number of the process,

$$\mathrm{Pe} = LV_c/\alpha. \qquad [6]$$

Inserting typical values for: L the length scale (~0.8 m), V_c the casting speed (*e.g.*, 3 m/min), and α the thermal diffusivity (~7×10^{-6} m^2/s) gives Pe of about 6×10^3, which greatly exceeds 1. This criterion breaks down at the meniscus region, ($L <$ ~2 mm), where this approach is already inaccurate because other important phenomena such as mold oscillation and fluid flow are being ignored.

A. *Simulation Domain*

The domain is a thin strip of finite elements extending through the thickness of the solidifying steel and liquid, as shown in Figure 3, and modeled as three rows of 400 finite elements each, 0.1 mm by 0.1 mm as shown in Figure 4.

A domain length of 40 mm was chosen to investigate shell thicknesses of up to about 15 mm, in order to have

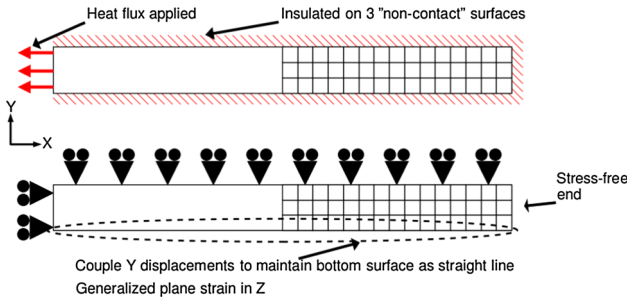

Fig. 4—Thermal and mechanical boundary conditions.

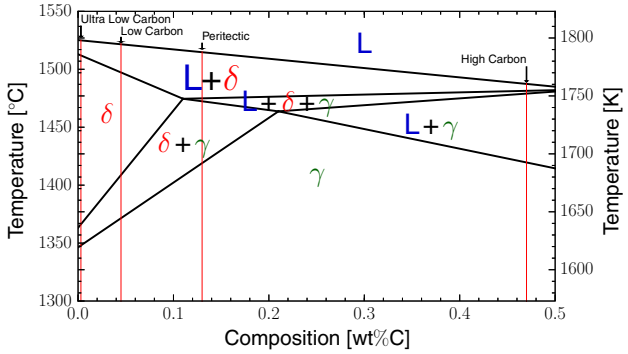

Fig. 5—Phase diagram for low-carbon steel showing approximate solidification path for four steel grades investigated.

enough liquid in the domain to avoid any influence from the far-field boundary condition.[50]

B. *Heat Transfer Model*

The two-dimensional transient heat conduction, Eq. [7], is solved for the temperature field in the solidifying shell:

$$\rho\left(\frac{\partial H}{\partial t}\right) = \nabla \cdot (k \nabla T), \qquad [7]$$

where ρ is the temperature-dependent mass density, k is the isotropic temperature-dependent thermal conductivity, and H is the temperature-dependent specific enthalpy which includes the latent heat of phase transformations, such as solidification and δ-ferrite to austenite. Two-dimensional elements were used to gain experience for future simulations with horizontal slice domains that include the strand corner region.

The instantaneous heat flux profiles, given by Eq. [5] and shown in Figure 2, are applied on the outer surface of the steel strand, while the three other surfaces are insulated, as shown in Figure 4.

The initial temperature of the domain for each case is set 5 K (5 °C) above the liquidus temperature of the steel grade, to facilitate comparison between grades. This fixed low superheat is typical of that removed from the wideface of slab casters, considering fluid flow in the liquid pool.[51] Fluid flow within the liquid pool creates a non-uniform superheat distribution in the melt, but this effect is minor when the pouring temperature is close to the liquidus temperature and thus is ignored in this work.

C. *Stress Model*

During initial solidification, the strains are on the order of only a few percent,[52] so the small strain assumption is adopted in this work. The mechanical behavior of the solidifying steel is governed by the quasi-static momentum balance given in Eq. [8].

$$\nabla \cdot \underline{\underline{\sigma}} + b = 0 \qquad [8]$$

where $\underline{\underline{\sigma}}$ is the second-order Cauchy stress tensor, and b is an applied body force (equal to zero for this work). Total strain rate is divided into elastic, inelastic, and thermal components,

$$\dot{\varepsilon} = \dot{\varepsilon}_{\text{el}} + \dot{\varepsilon}_{\text{ie}} + \dot{\varepsilon}_{\text{th}} \qquad [9]$$

where inelastic strain includes the combined effects of plastic strain and creep. Stress and strain are related by the unified constitutive equations for the steel grade, given in Section VI–E. Further details on the model formulation are given elsewhere.[23,53]

The constraint against bending is enforced kinematically: in the plane (about the z-axis) with coupling equations, and out of the plane (about the x- and y-axes) by using generalized plane strain finite elements. This technique ensures that the domain thickness and width uniformly expand or contract, modeling the effect of ferrostatic pressure by keeping the strand flat against the mold but without including the ferrostatic pressure itself. With this treatment, stress in the liquid is almost zero.

The mechanical behavior of the liquid is a challenge in modeling solidification with a fixed grid. Modeling the liquid as a Bingham plastic with a yield stress that is too weak can be difficult to converge numerically.[23] Conversely, if the liquid is modeled as too strong, convergence is easier, but may give unrealistic results by not allowing the solid to shrink as it would naturally. In this work, material points with fraction of liquid greater than zero are modeled as an elastic perfectly-plastic material with a yield strength of 10 kPa. Finally, the traction-free boundary condition at the end surface of the domain enables the domain length to change with time, thereby accounting for the flow of liquid into and out of the strand cross section, as it can in the real process. This treatment avoids the problems of unphysical constraint which otherwise would accompany the constant-mass condition that is inherent in the model.

D. *Phase Fraction Calculation*

Phase fractions are calculated as a function of temperature according to the steel composition, using the lever rule on a pseudo-binary phase diagram that approximates the real multicomponent alloy system. A pseudo-binary phase diagram is constructed based on 15 points in

temperature-composition space that change with alloying elements.[14,23] Figure 5 shows the high-temperature linearized phase diagram based on the alloy content of the typical low-carbon steel given in Table II.

In the non-equilibrium three-phase region, a rule for ternary systems is used.[54] This method provides the mass fractions of liquid, δ-ferrite, and austenite (γ) for each grade at any temperature during cooling. These phase fractions are then used to determine material properties as explained in Section VI.

E. *Solution Details*

The governing equations are solved using the finite element method[55] in ABAQUS/Standard (implicit).[56] The transient analysis was performed in two steps consisting of a 30-second heat transfer analysis, followed by a 30-second mechanical analysis. The implicit Euler method is used to integrate the transient heat conduction equation and the stress equilibrium equations are solved incrementally in time using Newton's method.[56] Within each time step, an efficient two-level (local–global) implicit method is used to integrate the highly non-linear constitutive equations at each material point, using 2×2 Gauss quadrature.[52] The Prandtl–Reuss equations are used to extend the uniaxial behavior defined by the constitutive models to three dimensions; further details of this method are provided elsewhere.[23,53,56]

Thermal boundary conditions are applied using the ABAQUS user subroutine DFLUX.[57] The calculated temperature field at each time step is input to the mechanical analysis to calculate the thermal strain. This "one-way coupled" method is appropriate for the uniform heat transfer with ideal mold contact conditions assumed here.[58] DC2D4 4-node linear diffusive heat transfer quadrilateral elements were used for the thermal analysis and CPEG4H 4-node hybrid bilinear generalized plane strain quadrilateral elements were used for the stress analysis.

The time step size was allowed to vary from 0.00001 to 1 second, which is controlled to keep the maximum temperature change per time step within 10 K (10 °C).[56] For the small 3×400 element mesh, simulations were run on one core of a Dell Precision T7600 workstation with 2 Intel Xeon 1.8 GHz quad-core processors and 64GB of DDR3 SDRAM and required about 2 hours of wall clock time each.

V. STEEL GRADES STUDIED

Four steel grades were investigated in this work: ultra-low carbon (ULC) with 0.003 wt pct C, low-carbon (LC) with 0.045 wt pct C, peritectic (P) with 0.13 wt pct C, and high-carbon (HC) with 0.47 wt pct C. The nominal composition of each grade is given in Table II and the phase transition temperatures are given in Table III. These grades were chosen to capture the range of different phase-dependent behavior of plain-carbon steel grades, *i.e.*, nearly pure iron, hypo-peritectic steel (non-peritectic steel on the low-C side of the peritectic reaction), peritectic steel, and hyper-peritectic steel. Other alloying elements were selected to make the grades typical of commercially produced steels.

Figure 6 shows the calculated phase fractions with temperature for all four grades investigated. As Figure 6 indicates, the liquid fraction decreases parabolically as the steel cools from its liquidus temperature. The transition temperatures and phase fractions predicted for these four steels match reasonably well with the CON1D software package[59] as well as with a more sophisticated microsegregation model developed from measurements.[60]

The ULC and LC grades transition fully into δ-ferrite from liquid, which persists for about 140 K (140 °C) for ULC and about 90 K (90 °C) for LC, before transitioning into austenite. The ULC has shorter transition regions than other steels, owing to the lack of alloy content. The higher carbon steels both experience a brief

Table II. Composition (Weight Percent) of the Four Steel Grades Examined in this Work

Steel	C	Mn	Si	S	P	Cr	Ni	Al	Ti	Cu
Ultra-Low Carbon	0.003	0.08	0.220	0.01	0.01	0.01	0.01	0.04	0.05	0.01
Low Carbon	0.045	0.20	0.015	0.01	0.01	0.01	0.01	0.04	0.05	0.01
Peritectic	0.130	0.50	0.020	0.01	0.01	0.01	0.01	0.04	0.05	0.01
High Carbon	0.470	0.75	0.005	0.01	0.01	0.01	0.01	0.04	0.05	0.01

Table III. Transition Temperatures (K (°C)) of the Four Steel Grades Examined in this Work

Steel	Pour	Liquidus	Solidus	Mushy Range	δ start	δ end	γ start
Ultra-Low Carbon	1810 (1537)	1805 (1532)	1794 (1521)	11	1794 (1521)	1652 (1379)	1636 (1419)
Low Carbon	1806 (1533)	1801 (1528)	1778 (1505)	23	1778 (1505)	1692 (1419)	1658 (1385)
Peritectic	1797 (1524)	1792 (1519)	1752 (1479)	40	1757 (1484)	1752 (1479)	1719 (1446)
High Carbon	1766 (1493)	1761 (1488)	1692 (1419)	69	1755 (1482)	1751 (1478)	1692 (1419)

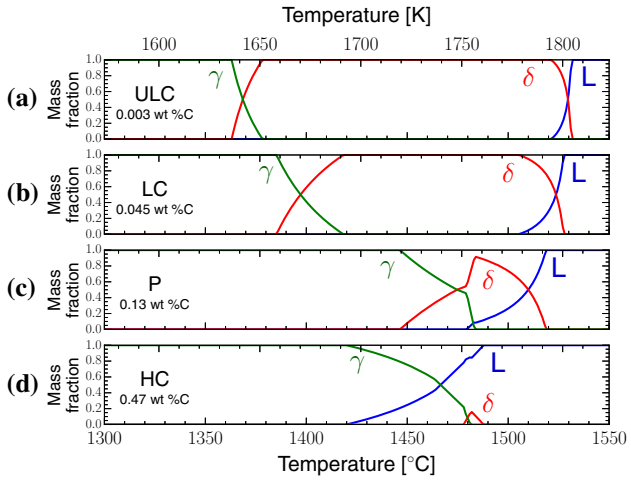

Fig. 6—Phase fractions for four steel grades investigated: (*a*) Ultra-Low carbon, (*b*) Low carbon, (*c*) Peritectic, (*d*) High carbon.

δ-phase region, which increases and decreases without reaching 100 pct. During the decrease in δ phase, the peritectic steel experiences the peritectic reaction, when δ ferrite and liquid both decrease sharply and form austenite.

VI. MATERIAL PROPERTIES

A. *Enthalpy and Heat Capacity*

The specific enthalpy (kJ/kg) curve used in this work to relate heat content and temperature is obtained by integrating the isobaric specific heat capacity (kJ/kg K) curve fit to measurements,[61]

$$\begin{aligned} H_l &= 824.6157T(\mathrm{K}) - 104,642.3 + \Delta H^l_{\mathrm{mix}} \\ H_\delta &= 0.8872T(\mathrm{K})^2 + 441.3942T(\mathrm{K}) + 50,882.26 \\ H_\gamma &= 0.0748901T(\mathrm{K})^2 + 429.8495T(\mathrm{K}) + 93,453.72 + \Delta H^\gamma_{\mathrm{mix}} \end{aligned} \quad , \quad [10]$$

where

$$\begin{aligned} \Delta H^l_{\mathrm{mix}} &= 18,125(\mathrm{pct\,C}) + 1,966,120\frac{(\mathrm{pct\,C})^2}{43.839(\mathrm{pct\,C}) + 1201.1} \\ \Delta H^\gamma_{\mathrm{mix}} &= 36,601(\mathrm{pct\,C}) + 1,907,930\frac{(\mathrm{pct\,C})^2}{43.839(\mathrm{pct\,C}) + 1201.1} \end{aligned} \quad . \quad [11]$$

Mixed phase regions are calculated using a weighted average based on the mass fraction of the phases present:

$$H = H_l f_l + H_\delta f_\delta + H_\gamma f_\gamma, \quad [12]$$

where f_l, f_δ, and f_γ are the mass fractions of liquid, δ-ferrite, and austenite phases, respectively. Equations [11] through [13] are plotted in Figure 7(b) for the four steel grades investigated in this work.

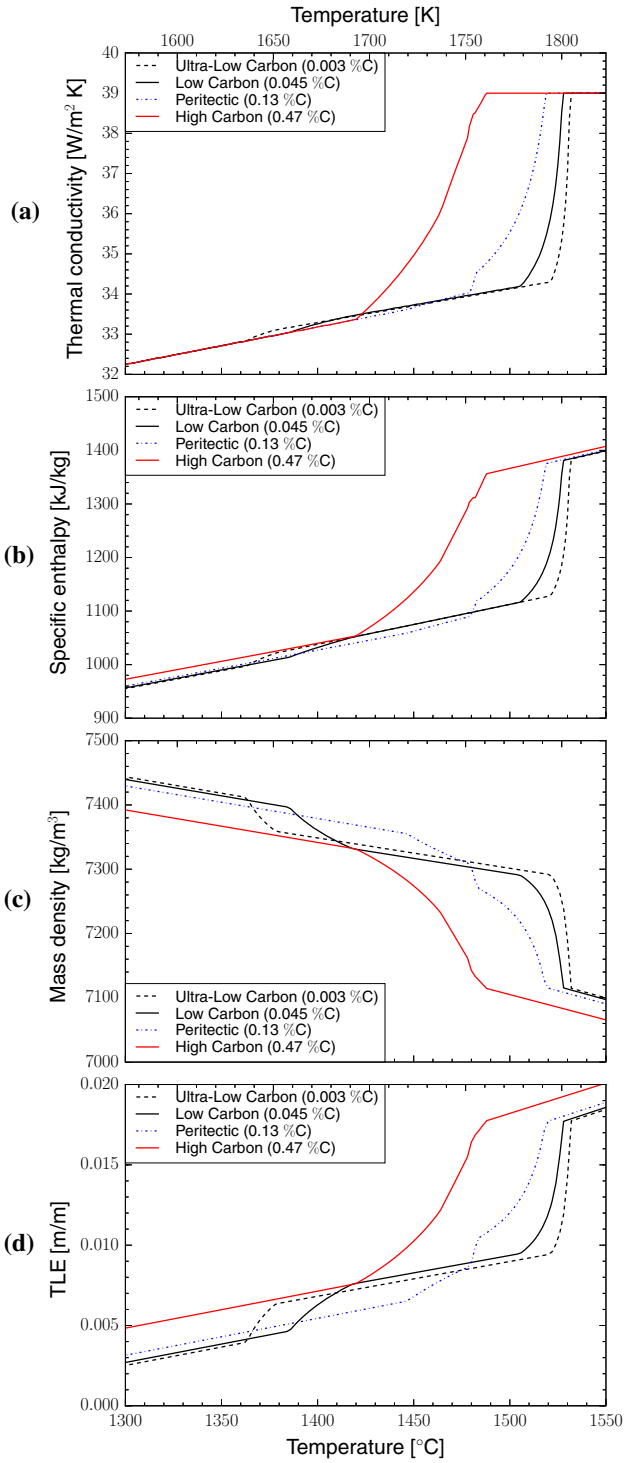

Fig. 7—Temperature-dependent properties of four steel grades investigated: (*a*) Thermal conductivity, (*b*) Specific enthalpy, (*c*) Mass density, (*d*) Thermal linear expansion.

B. *Thermal Conductivity*

The temperature-dependent thermal conductivity, k (W/m K) of plain carbon steel was fitted from measured data[62] and is given by

$$
\begin{aligned}
k_l &= 39.0 \\
k_\delta &= (21.6 + 0.00835T(^\circ C))(1 - (F_1(\text{pct C}^{F_2}))), \\
k_\gamma &= 20.14 + 0.00931T(^\circ C)
\end{aligned}
\quad [13]
$$

where

$$
\begin{aligned}
F_1 &= 0.425 - 0.0004385T(^\circ C) \\
F_2 &= 0.209 - 0.00109T(^\circ C)
\end{aligned}
\quad [14]
$$

Thermal conductivity of mixed phase regions is calculated using a mixture rule. Figure 7(a) shows the isotropic conductivity for the four steel grades investigated.

C. *Mass Density and Thermal Linear Expansion*

Curve fits for experimental data of mass density (kg/m^3)[19,63] yields

$$
\begin{aligned}
\rho_l &= 7100 - 73.2(\text{pct C}) - (0.828 - 0.0874(\text{pct C}))(T(^\circ C) - 1550) \\
\rho_\delta &= \frac{-0.4724T(^\circ C) + 8,010.71}{(1.0 - 0.01(\text{pct C})(1.0 + 0.01343(\text{pct C}))^3} \\
\rho_\gamma &= \frac{-0.5091T(^\circ C) + 8,105.91}{(1.0 - 0.01(\text{pct C})(1.0 + 0.008317(\text{pct C}))^3}
\end{aligned}
\quad [15]
$$

In regions with mixed phases, the mass density is calculated using a phase-fraction weighted average of the phases present. The temperature-dependent mass density of the four steel grades investigated is shown in Figure 7(c).

The Thermal Linear Expansion (TLE) function is obtained from solid-phase mass density measurements[61] and liquid density measurements,[63] and is given by Eq. [16] using the values from Eq. [15] depending on the phases present.

$$
\text{TLE} = \sqrt[3]{\frac{\rho(T_0)}{\rho(T)}} - 1 \quad [16]
$$

where T is the current temperature, and T_0 is a reference temperature set to 1780 K (1507 °C) for all grades in this work. Figure 7(d) compares the TLE curves of all four grades. The steep drops for each grade correspond to phase changes. In this work, the TLE is assumed to be isotropic.

D. *Elastic Constants*

The temperature-dependent Young's modulus data[64] used in this work is shown in Figure 8, and is the same for all grades.

The Young's modulus of the liquid phase is set to 10 GPa. The Poisson's ratio is taken constant at $\nu = 0.3$ in this work. The measured Poisson's ratio that approaches about 0.5 at high temperatures is achieved with this model, by considering the large extent of incompressible creep strain ($\nu = 0.5$) that accompanies the elastic strain during tests.[65]

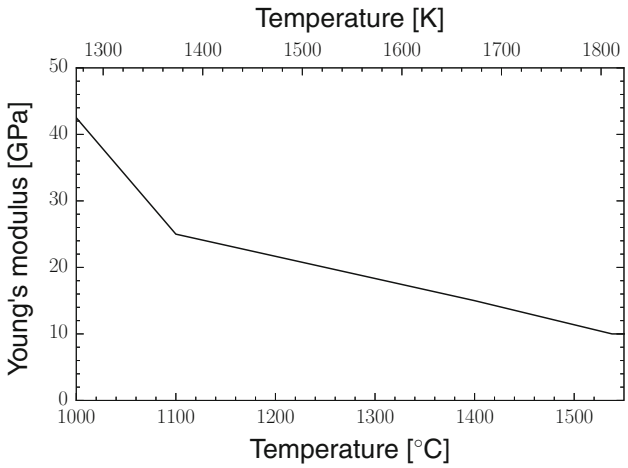

Fig. 8—Temperature-dependent Young's modulus of steel.

E. *Constitutive Models*

The elastic visco-plastic constitutive model used here includes both strain-rate-independent plasticity and time-dependent creep; as creep is significant at the high temperatures of the solidification processes and is indistinguishable from plastic strain.[23] The inelastic behavior of each steel phase is described by its own constitutive model, and isotropic behavior is assumed.

When the liquid fraction of a material point is greater than zero, a perfectly-plastic material model is used, with $\sigma_{\text{yield}} = 10$ kPa.[66] This liquid strength introduces a small error that increases with increasing yield strength, increasing size of the liquid portion of the domain, and increasing elastic modulus.

The δ-ferrite is modeled with the Zhu modified power law[23,67]:

$$
\dot{\bar{\varepsilon}}_{\text{in}-\delta}(1/\text{s}) = 0.1F_\delta|F_\delta|^{n-1}, \quad [17]
$$

where

$$
\begin{aligned}
F_\delta &= \frac{C\bar{\sigma}}{f_C\left(\frac{T(\text{K})}{300}\right)^{-5.52}(1 + 1000|\bar{\varepsilon}_{\text{in}}|)^m} \\
f_C &= 1.3678 \times 10^4(\text{pct C})^{-5.56\times10^{-2}} \\
m &= -9.4156 \times 10^{-5}T(K) + 0.349501 \\
n &= (1.617 \times 10^{-4}T(K) - 0.06166)^{-1}
\end{aligned}
\quad [18]
$$

The austenite phase uses model III from Kozlowski[68]:

$$
\dot{\bar{\varepsilon}}_{\text{in}}(1/\text{s}) = f_{\text{pct C}}|F_\gamma|^{f_3-1}F_\gamma \exp\left(\frac{-4.465 \times 10^4}{T(\text{K})}\right) \quad [19]
$$

where accumulated inelastic strain, $\bar{\varepsilon}_{\text{in}}$, acts as the structure parameter; F_γ acts as a strain-hardening back-stress term to achieve the Bauschinger effect and plastic shakedown in the mechanical behavior during cyclic loading[69]

Table IV. Properties Used in Verification Problem

Property	Value	Unit
Thermal conductivity	33	W/m K
Mass density	7500	kg/m^3
Young's modulus (solid)	4000	MPa
Young's modulus (liquid)	1400	MPa
Poisson's ratio	0.3	—
Thermal expansion	2×10^{-5}	1/K
Pour temperature	1769 (1496)	K (°C)
Fixed wall temperature	1273 (1000)	K (°C)
Liquidus temperature	1768.1 (1495.1)	K (°C)
Solidification temperature	1768 (1495)	K (°C)
Solidus temperature	1767.9 (1494.9)	K (°C)
Latent heat	272	kJ/kg
Specific heat capacity	661	J/kg K

$$
\begin{aligned}
F_\gamma &= C\bar{\sigma} - f_1\bar{\varepsilon}_{\text{in}}|\bar{\varepsilon}_{\text{in}}|^{f_2-1} \\
f_1 &= 130.5 - 5.128 \times 10^{-3}T(\text{K}) \\
f_2 &= -0.6289{+}1.114 \times 10^{-3}T(\text{K}) \\
f_3 &= 8.132 - 1.54 \times 10^{-3}T(\text{K}) \\
f_{\text{pct C}} &= 4.655 \times 10^4 + 7.14 \times 10^4(\text{pct C}) + 1.2 \times 10^5(\text{pct C})^2
\end{aligned}
\qquad [20]
$$

where C takes on a value of 1 or -1 depending on the sign of the effective inelastic strain.[52] Eqs. [18] and [19] were developed to match tensile-test measurements[20] and creep test data[22] for austenite, and Eqs. [16] and [17] for ferrite. Further details of these two models can be found elsewhere.[23,52]

The δ-ferrite is approximately one order of magnitude weaker than austenite at the same temperature[20]; so a weighted mixture rule is not appropriate in regions containing both phases.[52] Thus, the δ-ferrite constitutive model is used in mixed phase regions whenever the fraction of δ-ferrite is greater than 10 pct.

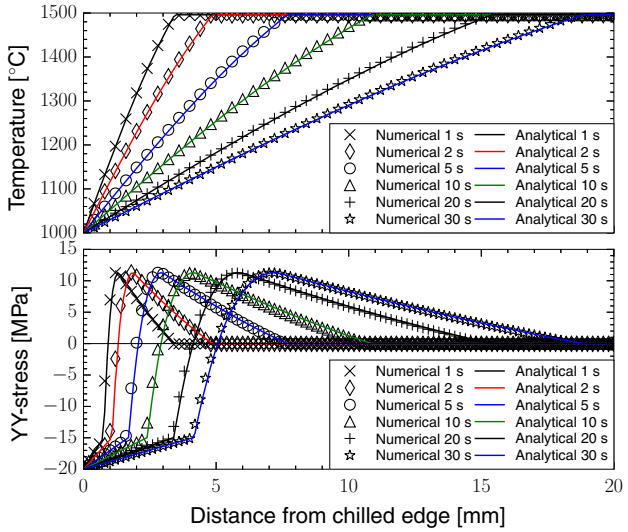

Fig. 9—Comparison of Weiner & Boley and ABAQUS temperature and stress distributions through the shell.

VII. MODEL VERIFICATION AND VALIDATION

Accurate models require: (1) verification against a test problem with a known solution, to demonstrate accurate model implementation and resolution, and (2) validation with experimental measurements to show that the model formulation, properties, and input data are reasonable.

The model in this work was verified using the analytical solution derived by Weiner and Boley.[70] This problem considers solidification from a fixed-temperature boundary of a semi-infinite plate, consisting of an elastic-perfectly-plastic material that is initially liquid. The plate is constrained against bending but otherwise free to shrink. In this work, the constants and parameters used to approximate this simplified verification problem are depicted in Table IV.

The domain is the same thin and narrow strip of 400 elements through the plate thickness used in this work to investigate the effect of steel grade. The surface is suddenly quenched at time zero, which causes the domain to start cooling. Because the liquid has negligible strength, and thus carries negligible stress, during this initial cooling step, the surface shrinks almost stress-free. As time progresses, the rest of the domain cools and the hot interior tends to shrink more than the colder surface. As explained in Section IV, the domain is constrained to keep the upper and lower edges parallel. This constraint opposes the tendency of the domain to shrink into a "wedge," which generates tension in the interior, with corresponding compression arising in the surface region to maintain equilibrium. The average stress must be zero because the plate edges are unconstrained.

Results of the numerical and analytical solutions are compared in Figure 9. The temperature and stress profiles are plotted along the lower edge of the domain from the chilled end toward the free end. The temperature in the liquid remains constant, while the temperature profile through the solid has an almost constant gradient that decreases with time. The stress profile shows the expected behavior of compression at the

surface increasing to tension near the solidification front, and decreasing to zero in the liquid. Both the temperature and stress results match closely at all positions and times, which verifies the model.

For model validation, the thermal–mechanical model in this work was previously compared with the experimental measurements of force on a solidifying 0.315 pct C steel shell in a Submerged Split-Chill Contraction Test apparatus (Fig. 11 in Reference 71). The model predicts zero force until 100 pct solid is reached, while the measurements show some strength in the liquid at small, non-zero, liquid fractions. Once fully solidified, the model agrees both qualitatively and quantitatively within 10 pct until the measured force drops due to internal failure mechanism(s), which are not included in the model. In a separate modeling study, the model in this work was found to produce similar mechanical behavior to that using the Anand constitutive model for 0.27 pct C steel.[52] However, it is clear that further experimental validation of the model in this work is needed, especially for different steel grades and conditions.

VIII. MESH RESOLUTION STUDY

A mesh study was conducted for realistic solidification of LC steel with standard heat flux, to demonstrate that the solution is independent of the discretization. The number of elements through the solidification direction (x) was varied, while three elements were maintained through the domain thickness. The element aspect ratio was fixed at 1 by keeping all elements square. For example, the 3 × 10 element mesh has 4-mm square elements, so the domain thickness was 12 mm.

Figure 10 shows the results for six different mesh refinements after 10 seconds of solidification. These results indicate that while 1, 2.5, and 4 mm elements can accurately reproduce the temperature history, shown in Figure 10(a), a much more refined mesh is necessary to properly resolve the stress and strain behavior, which is shown in Figure 10(b) through (d).

While 4 mm elements capture the expected behavior of compression at the surface and tension toward the solidification front, the accuracy of the stress

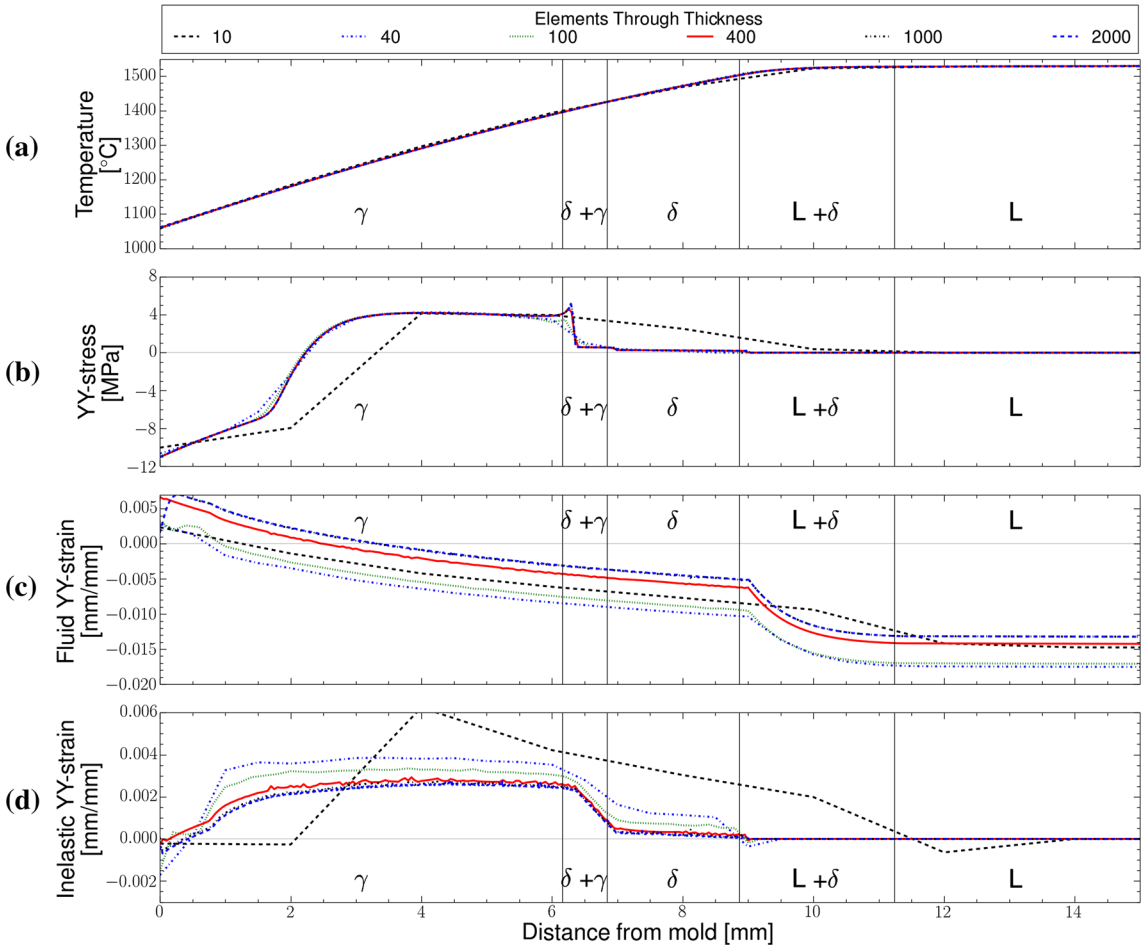

Fig. 10—Mesh study results through shell thickness for low-carbon steel (0.045 pct C) – 10 s below meniscus: (*a*) Temperature, (*b*) Y-stress, (*c*) Fluid strain, (*d*) Inelastic strain.

predictions depends strongly on the number of elements through the mushy zone and other phase transition regions, where stress changes sharply. The size of the mushy zone is strongly grade-dependent and can vary by almost an order of magnitude. For the LC steel shown, the mushy zone is only about 2 mm wide at 10 seconds and with elements larger than that size, the mushy zone could be contained within a single element. In addition, the δ-ferrite→austenite region is only about 1 mm wide, so the 1-mm element mesh just barely captures the details. This mesh coarseness causes accuracy problems, because properties and thermal–mechanical behavior are very non-linear during phase changes.

The grid-independent stress results, shown in Figure 10(b), are quite accurate. The liquid region has almost zero stress, although there is some slight compression due to the artificial yield stress of the liquid combined with the domain shrinkage squeezing the liquid toward the stress-free end upon surface solidification.

The inelastic strain results, shown in Figure 10(d), are the least accurate. The 4-mm element mesh captures the general behavior in the austenite near the surface, but overpredicts the strain in the mushy zone and into the liquid. Thus, mesh selection should be based on achieving accurate mechanical behavior, including the inelastic strain. Sufficient elements are needed to resolve the phase transition regions, especially if they are areas of interest.

In this work, 0.1 mm elements were chosen (3 × 400 element mesh) to capture the relevant stress phenomena, to within 0.3 pct and inelastic strain within 0.9 pct, at the maximum location, at 10 seconds, while retaining reasonable computation speed.

IX. TYPICAL RESULTS FOR LC STEEL

Typical results for low-carbon steel are used to show the thermal–mechanical behavior predicted by the model. Figure 11 shows the temperature, thermal strain, fluid strain, and inelastic strain, and the stress results are presented in Figure 10(b).

A breakdown of the total strain into its components of elastic, thermal, fluid, and inelastic strain profiles at 10 seconds below the meniscus is given in Figure 12.

Stress and strain components are shown in the direction tangential to the surface (Y–Y component).

A. *Shell Growth and Temperature*

The temperature contours in Figure 11(a) show that shell growth, s, follows the well-known $s = k\sqrt{t}$ behavior. At 30 seconds, the low-carbon steel has a total shell thickness of about 16 mm with the mushy zone extending just 3 mm beyond that. The austenite (γ) portion of the shell is slightly more than 10 mm thick, extending inwards from the surface; the δ-ferrite region is about 3.5 mm thick. The $\delta \rightarrow \gamma$ transition region remains only about 1 mm for the entire simulation.

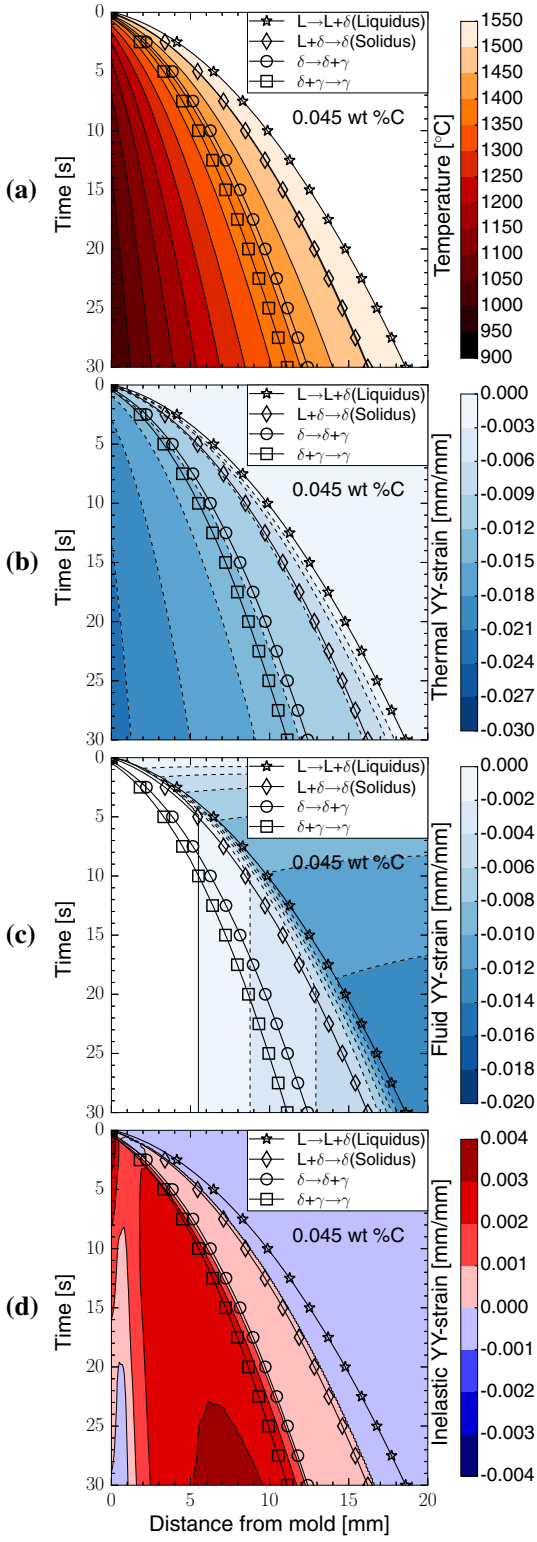

Fig. 11—0.045 pct C low–carbon steel contours: (*a*) Temperature, (*b*) Thermal strain, (*c*) Fluid strain, (*d*) Inelastic strain.

B. *Stress*

Compression develops at the surface and tension is generated at the solidification front, as discussed in the Weiner and Boley problem. Compression at the surface

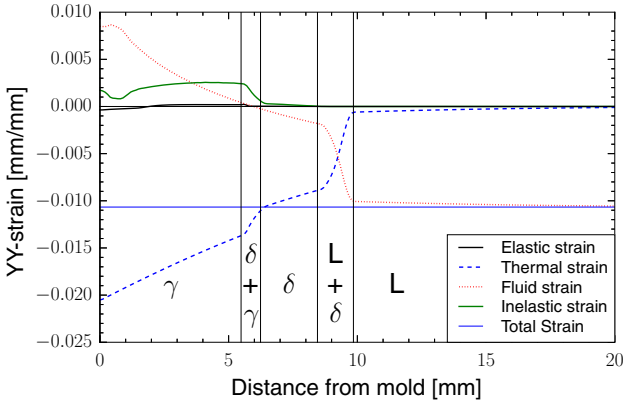

Fig. 12—Typical strain distribution through the shell thickness for low-carbon steel (0.045 pct C) – 10 s below meniscus.

increases with time, as the entire shell attempts to further shrink and is opposed by the growing region of colder stronger solid steel.

C. *Elastic Strain*

Elastic strain is directly proportional to the stress and displays compression at the surface with tension toward the solidification front. Most of the stress and elastic strain are carried in the austenite, with very little observed in the δ-ferrite region due to the lower strength of the phase. Elastic strains are always less than ~0.05 pct,[72] which is very small relative to the other strains.

D. *Thermal Strain*

The thermal strain dominates the mechanical behavior, going further into compression with time, *i.e.*, decrease in temperature. This behavior is accentuated through transition regions, where the changes in density are most abrupt and drive negative thermal expansion; the largest being the initial contraction of liquid-to-solid transformation.

E. *Fluid Strain*

The fluid strain (also called "flow strain"[23]) is the inelastic strain generated in the liquid, which occurs to accommodate the domain shrinkage, and represents a measure of liquid feeding. Feeding difficulties can lead to porosity between dendrites[73] if the liquid is unable to flow to fill the interdendritic spaces. After solidification is complete, the fluid strain remains constant with time, and further inelastic strain builds up in the solid phases.

Within the liquid region, the fluid strain is always compressive, which indicates flow out of the region. This compression is a real consequence of the constraints on the domain, which require the upper and lower edges to remain parallel; shrinkage of the solid portion of the domain squeezes the liquid portion of the domain as well, causing liquid to flow outwards away from the solidification front. In addition to generating fluid strain, this squeezing initially causes the length of the domain to increase rapidly (as the rapid surface cooling causes shrinkage of the strong cold shell at the surface, which dominates the strength and behavior of the entire domain). Later, the domain length shrinks, as the surface cools and shrinks more slowly than the interior.

F. *Inelastic Strain*

Low levels of tensile inelastic strain begin to develop in the δ-ferrite region and increases drastically during the transition to austenite. At the surface, the rapid initial solidification and very thin mushy zone causes more compressive thermal strain, tensile stress, and tensile inelastic strain. In the case of the low-carbon steel shown, this tensile inelastic strain persists at the surface, even after 10 seconds.

G. *Total Strain*

Driven largely by the thermal strain, the total strain becomes increasingly compressive during solidification as the domain cools and shrinks. The total strain naturally remains constant through the shell thickness and accompanying liquid in the domain, as required for a plate that is constrained from bending. Total strain is the important quantity to match when designing mold taper.

X. EFFECT OF STEEL GRADE

The temperature, stress, and strain results of the four different steel grades are compared in Figures 13, 14, 15, 16, 17. The peritectic steel grade was simulated with both the same "higher" heat flux as the others, and with the low heat flux, more typical of this grade in practice.

A. *Shell Growth and Temperature*

Comparing the peritectic steel results in Figures 13(c) and (d) shows that increasing heat flux causes the shell thickness to increase by about 20 pct (represented by corresponding increases in both the solidus and liquidus contour positions).

At the same time, the higher heat flux also causes a lower surface temperature, owing to the steeper temperature gradient, as shown in Figure 14.

Increasing carbon content causes increased thickness of the mushy zone, according to the increasing temperature range between the liquidus and solidus temperatures, as shown in the left side of Figure 13. With the same superheat, the liquid temperature decreases with increasing carbon content, as shown in the top right of Figure 14, so the temperature profiles of the four grades become correspondingly lower.

The effect of steel grade on shell thickness is complicated, because it depends on the thermal properties, the heat flux, and the definition of shell thickness. Except for the peritectic steel, increasing the carbon content increases the liquidus thickness and decreases the solidus thickness, due to the increase in mushy zone thickness.

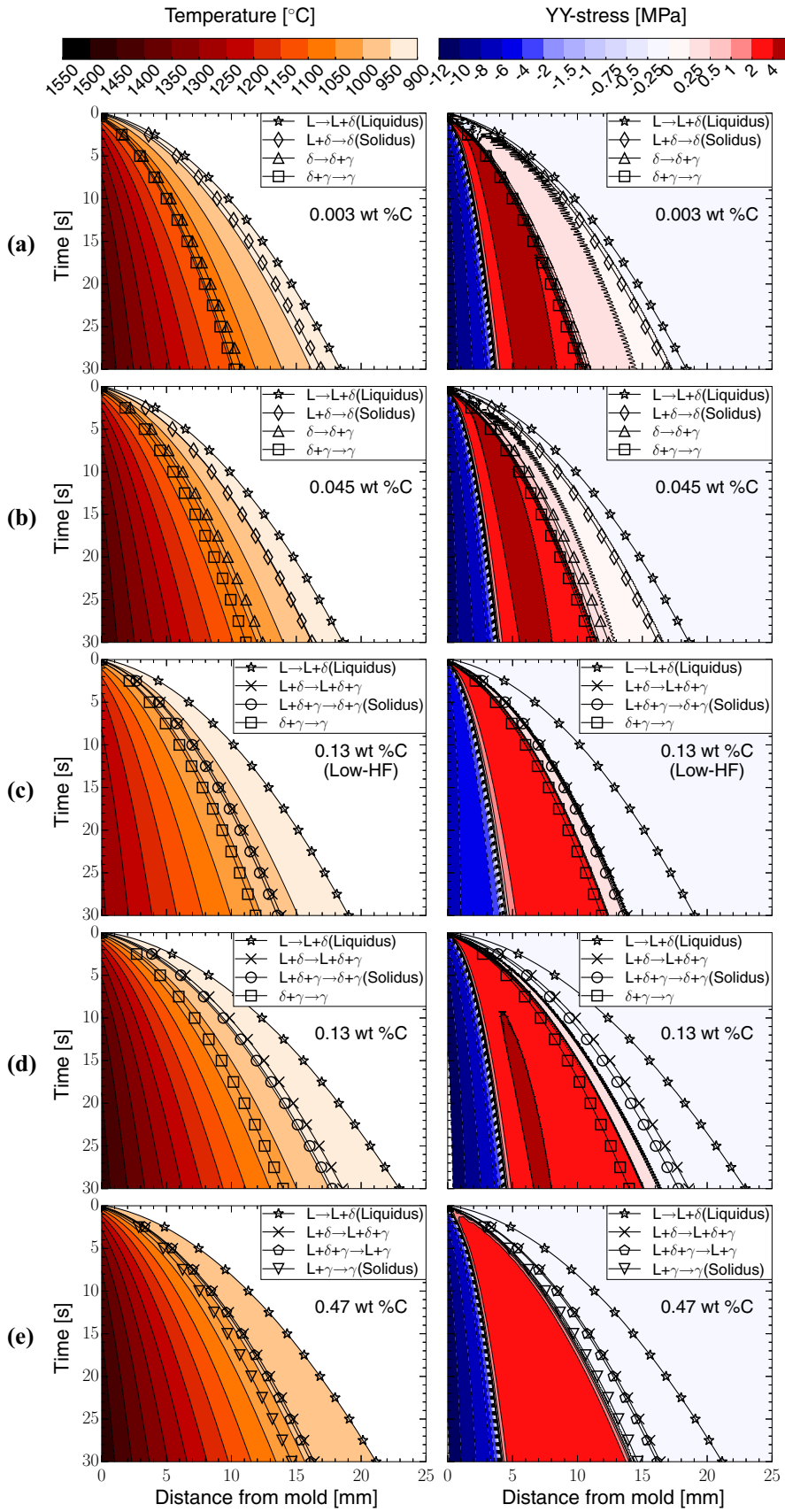

Fig. 13—Temperature and Y-stress contours for five casting situations investigated: (*a*) Ultra-low-carbon steel with Standard HF, (*b*) Low-carbon steel with Standard HF, (*c*) Peritectic steel with Standard HF, (*d*) Peritectic steel with Low HF, (*e*) High-carbon steel with Standard HF.

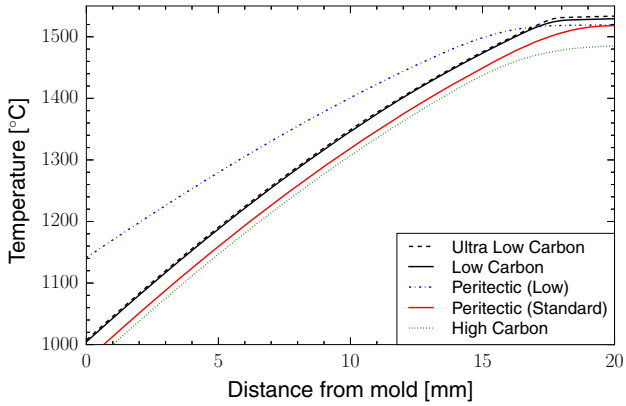

Fig. 14—Temperature profile through the shell thickness at 30 s for five casting situations investigated.

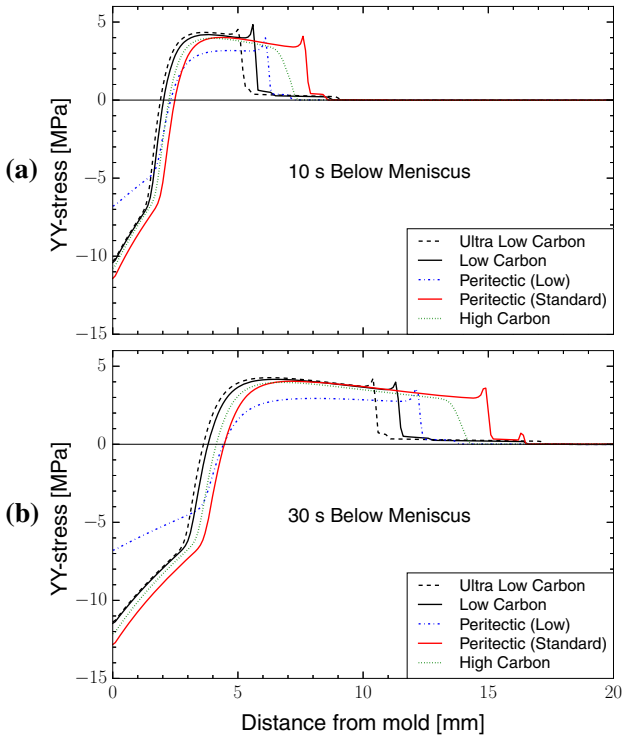

Fig. 15—Y-stress profiles through shell thickness for five casting situations investigated: (*a*) 10 s, (*b*) 30 s.

B. *Stress*

For all four steels, the general stress profile exhibits compression at the surface, increasing to tension near the solidification front, and down to zero in the liquid, as shown in Figures 13 and 15. At early times in all steels, however, a brief tensile peak appears at the surface, due to the rapid cooling and shrinkage, as shown in Figure 16(b). This rapid shrinkage generates a corresponding very mild compression region inside the δ-ferrite for a brief period, which can be seen in the top left of Figures 15(a) and (b) stress frames.

As time increases beyond 2 seconds, surface stress becomes compressive in all steel grades. As the steel continues to cool and strengthen, the magnitude of this surface compression increases. For the same reason, decreasing the heat flux (in the peritectic steel) causes higher temperatures and lower absolute stress levels, both at the surface and in the interior.

Figure 15 shows the low stress in the δ-ferrite whenever that phase appears, which is due to its low strength and inability to carry any significant load. Moving towards the left, a sharp increase in strength from δ-ferrite to austenite is observed, which is accompanied by a pointed peak where the crystal structure changes from BCC to FCC. Although this peak is not a numerical error, it is an artifact that disappears when the phase transition occurs over a wide temperature range. Naturally, this peak is missing from high-carbon steel, which has no delta phase, so its stress transition is smooth across the austenite near the solidification front.

C. *Strain*

Contours of the thermal, fluid, and inelastic strain components are compared for the four steel grades in Figure 16.

The dominant component, thermal strain, increases in magnitude as temperature decreases. Thus, the greatest magnitude thermal strain is found at the surface, where it increases with decreasing carbon content.

The fluid strain evolution in all grades is similar to that discussed for low-carbon steel previously. Fluid strain is always negative, indicating shrinkage. The greatest magnitude fluid strain is observed in the peritectic steel with standard heat flux, owing to the greater shrinkage of this grade for the same high heat flux.

The results in Figure 17 show the initial tensile peaks and histories of the inelastic strain decrease in magnitude with increasing carbon content. These increased tensile peaks result in the lower carbon steel grades (below 0.13 pct C) remaining with positive inelastic strain at the surface, even after 30 seconds when the higher carbon grades have become negative. These findings agree with previous results.[26] The peaks are likely caused by the high initial inelastic strain that arises in the weak δ-ferrite phase during the initial rapid cooling, shrinkage, and short tensile–stress peak that arises at the surface, as observed in Figure 17(b). The inelastic strain peaks persist longer in correspondence with the extent of the short tensile peak.

XI. GRADE-BASED TAPER PRACTICE

The results of this work indicate some of the qualitative differences between different alloys, and have implications for optimal taper practice in continuous casting. Proper taper practice is important to mold operation to ensure uniform heat transfer between the mold and shell and to reduce the likelihood of surface defects and breakouts. Shrinkage of the steel shell is accommodated by tapering the mold to maintain contact between the edges of the shell and the mold walls. Insufficient taper can lead to reduced or non-uniform heat transfer between the strand and the mold,

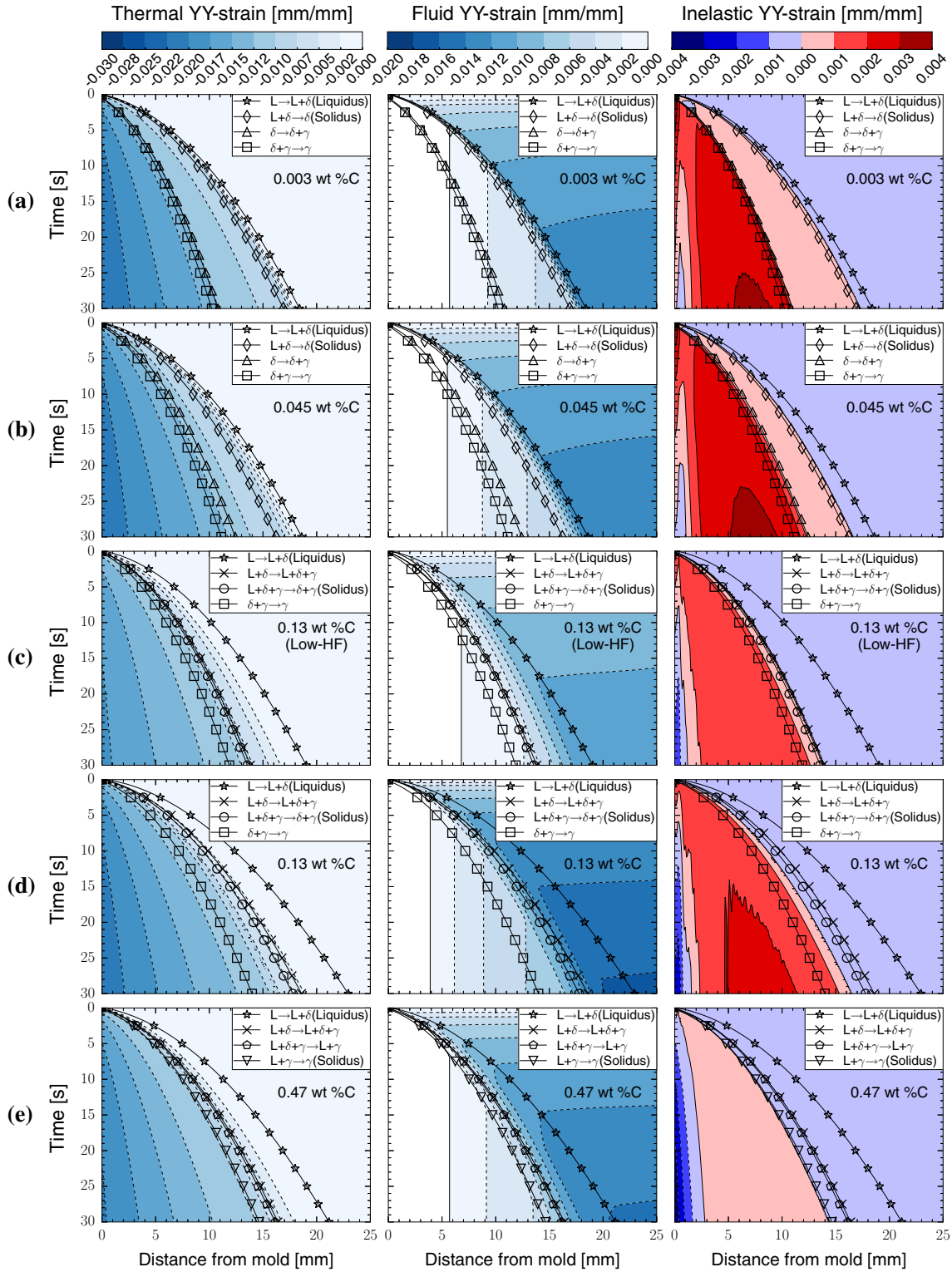

Fig. 16—Thermal, Fluid, and Inelastic strain contours for five casting situations investigated: (*a*) Ultra-low-carbon steel with Standard HF, (*b*) Low-carbon steel with Standard HF, (*c*) Peritectic steel with Standard HF, (*d*) Peritectic steel with Low HF, (*e*) High-carbon steel with Standard HF.

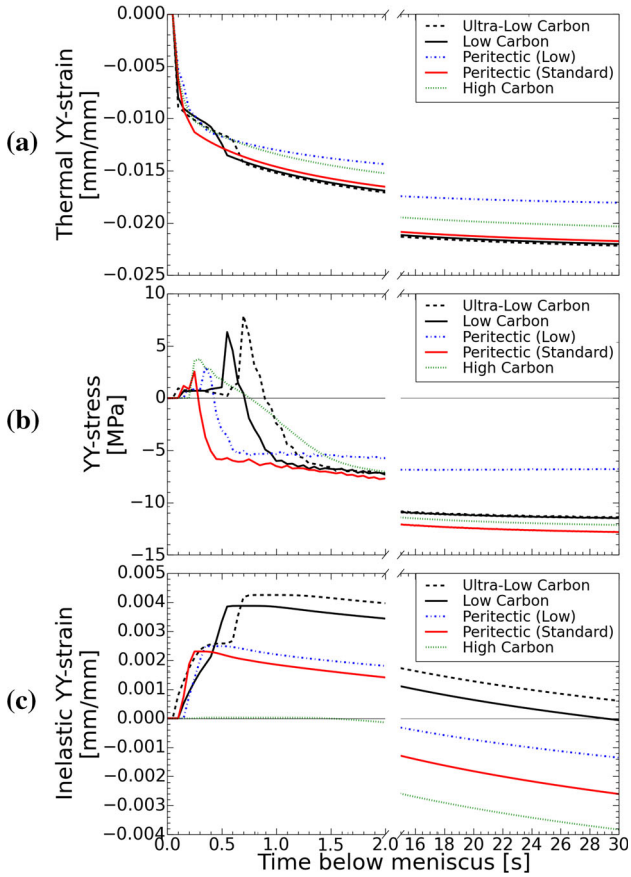

Fig. 17—Surface profiles for five casting situations investigated: (*a*) Thermal strain, (*b*) Y-stress, (*c*) Inelastic strain.

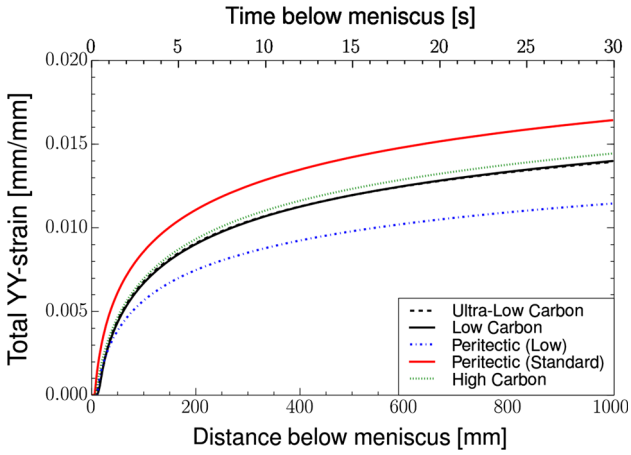

Fig. 18—Ideal taper profile for five casting situations investigated.

which can lead to corner rotation, shell thinning, and narrow face bulging.[74] Excessive taper can lead to accelerated mold wear, or even buckling of the shell.[74] Both taper problems can cause gutter, longitudinal cracks, and breakouts.[74]

Figure 18 shows the ideal taper profiles for all casting situations, calculated with a casting speed of 2 m/min. These taper profiles are based on the total shrinkage of the shell, which is indicated by the total Y–Y strain and increases at a decreasing rate with time down the mold. This shrinkage is controlled mainly by the drop in surface temperature because the shell at the surface is coldest and strongest. All of the steel grades experience more shrinkage near the top of the mold, because of this drop in temperature, so the ideal taper profile should be curved (convex toward the molten steel).

For the same heat flux, the peritectic steel experiences the greatest shrinkage and so it requires more taper, while the other three steels have similar, but lower ideal taper profiles. This large shrinkage accompanies the δ-ferrite to austenite phase transformation, and occurs in the solid at high temperature in the peritectic steel, while the shell is still hot and weak, and unable to resist the shrinkage. However, with decreased heat flux, that is typical of the real commercial process, the peritectic steel experiences about 30 pct less shrinkage and thus needs less taper. The dependence of taper on heat flux indicates that casting speed and mold powder should have a greater effect on ideal taper than steel grade, which is consistent with previous findings.[29]

This simple model can help in the calculation of taper profiles for different steel grades to maintain the desired contact over the entire mold length. While fixed linear taper of the mold is a common practice in industry, it is clear that the ideal shrinkage profile of the shell is non-linear, which agrees with previous work.[75] The total strain profiles presented here are only a rough starting point for designing ideal taper. Designing taper in a real operating caster requires consideration of many other factors such as friction with the mold walls, creep expansion of the shell width due to ferrostatic pressure on the unmodeled mold faces, mold distortion,[76] and mold wear.[77]

XII. CONCLUSIONS

A thermal–mechanical model of solidification of a flat steel shell has been developed and applied to investigate the effect of steel grade on temperature, stress, strain, ideal taper, and shell development during the early stages of solidification in a frictionless mold. The model features realistic boundary conditions based on previous literature, and realistic thermal and mechanical properties that vary with temperature, phase fraction, and carbon content. Four different steel grades were investigated: ultra-low carbon (0.003 pct C), low carbon (0.04 pct C), peritectic (0.13 pct C), and high carbon (0.47 pct C), simulating 30-second dwell times. Specific findings are as follows:

- The initial shell solidification rate increases with carbon content, for the conditions of fixed heat flux profile used in this work.
- All steel grades follow the same general solidification behavior of compression at the surface with tension toward the solidification front.
- Thermal strain dominates the mechanical behavior. Initially, fast cooling causes tensile stress and inelastic strain at the surface of the shell, with slight complementary compression beneath the surface,

especially with lower carbon content. As the cooling rate decreases, the surface then reverses into compression, with a tensile region developing subsurface.
- In all steel grades, persistent positive inelastic strain at the surface is likely caused by the brief tensile peaks arising from the rapid initial surface cooling and accompanying steep thermal gradient.
- Initial tensile inelastic strain peaks and the subsequent inelastic strain history decrease in magnitude with increasing carbon content.
- The stress generated in the δ-ferrite phase is always very small, owing to the low strength of this phase.
- More stress and inelastic strain are eventually generated in the high-carbon steel, because it is mainly composed of high-strength austenite.

XIII. FUTURE WORK

This work is the first step in the development of a comprehensive transient 3D model of thermal–mechanical behavior during continuous casting of steel slabs, which will include mold distortion, corner effects, and non-uniform heat flux around the mold perimeter. In this modeling approach, the properties of different steel grades depend mainly on the phase fraction histories. This enables predictions of any steel grade knowing only the phase fraction histories, and so does not require extensive experimental testing. Validation of this approach with measurements would be helpful, and is intended as future work.

ACKNOWLEDGMENTS

The authors wish to acknowledge the financial support of the Continuous Casting Consortium at the University of Illinois at Urbana–Champaign and the National Science Foundation (Grant Number: CMMI-1300907).

REFERENCES

1. M. Rappaz: *Curr. Opin. Solid State Mater. Sci.*, 2016, vol. 20, pp. 37–45.
2. C. Beckermann: *Int. Mater. Rev.*, 2002, vol. 47, pp. 243–61.
3. M. Asta, C. Beckermann, A. Karma, W. Kurz, R. Napolitano, M. Plapp, G. Purdy, M. Rappaz, and R. Trivedi: *Acta Mater.*, 2009, vol. 57, pp. 941–71.
4. W.J. Boettinger, S.R. Coriell, A.L. Greer, A. Karma, W. Kurz, M. Rappaz, and R. Trivedi: *Acta Mater.*, 2000, vol. 48, pp. 43–70.
5. W.T. Lankford: *Metall. Trans.*, 1972, vol. 3, pp. 1331–57.
6. M.B. Santillana: Ph.D. Thesis, Delft University of Technology, 2013.
7. S.N. Singh, and K.E. Blazek: *J. Met.*, 1974, pp. 17–27.
8. S.C. Moon: Ph.D. Thesis, University of Wollongong, 2015.
9. M.M. Wolf and K. Kurz: *Metall. Mater. Trans. B*, 1981, vol. 12B, pp. 85–93.
10. J. Konishi, M. Militzer, I.V. Samarasekera, and J.K. Brimacombe: *Metall. Mater. Trans. B*, 2002, vol. 33B, pp. 413–23.
11. P. Presoly, R. Pierer, and C. Bernhard: *Metall. Mater. Trans. A*, 2013, vol. 44A, pp. 5377–88.
12. E. Wielgosz and T. Kargul: *J. Therm. Anal. Calorim.*, 2015, vol. 119, pp. 1547–53.
13. K.E. Blazek, O. Lanzi, and H. Yin: in *AISTech - Iron Steel Technol. Conf. Proc.*, Pittsburgh, PA, 2008, pp. 609–25.
14. A. Kagawa and T. Okamoto: *Mater. Sci. Technol.*, 1986, vol. 2, pp. 997–1008.
15. J.O. Andersson, T. Helander, L. Hoglund, P. Shi, and B. Sundman: *Calphad*, 2002, vol. 26, pp. 273–312.
16. C.W. Bale, P. Chartrand, and S.A. Degterov: *Calphad*, 2002, vol. 26, pp. 189–228.
17. J. Miettinen, S. Louhenkilpi, H. Kytönen, and J. Laine: *Math. Comput. Simul.*, 2010, vol. 80, pp. 1536–50.
18. R.D. Pehlke, A. Jeyarajan, and H. Wada: *Summary of Thermal Properties for Casting Alloys and Mold Materials*, University of Michigan, Ann Arbor, MI, 1982.
19. A. Jablonka, K. Harste, and K. Schwerdtfeger: *Steel Res.*, 1991, vol. 62, pp. 24–33.
20. P.J. Wray: *Metall. Mater. Trans. A*, 1984, vol. 15A, pp. 2059–73.
21. P.J. Wray: *Metall. Mater. Trans. A*, 1984, vol. 15A, pp. 2041–58.
22. M. Suzuki and Y. Yamaoka: *Mater. Trans.*, 2003, vol. 44, pp. 836–44.
23. C. Li and B.G. Thomas: *Metall. Mater. Trans. B*, 2004, vol. 35B, pp. 1151–72.
24. J. Sengupta, C. Ojeda, and B.G. Thomas: *Int. J. Cast Met. Res.*, 2009, vol. 22, pp. 8–14.
25. Y. Meng, C. Li, J.T. Parkman, and B.G. Thomas: in *International Conference on Modeling Casting Welding and Advanced Solidification Processes*, M. Rappaz, ed., The Minerals, Metals & Materials Society, Charlotte, NC, 2004, pp. 33–39.
26. B.G. Thomas and J.T. Parkman: in *Thermec '97 International Conference on Thermomechanical Processes Steel Other Mater.*, Wollongong, Australia, TMS, 1997, pp. 2279–85.
27. R.J. Dippenaar, I.V. Samarasekera, and J.K. Brimacombe: *ISS Trans.*, 1986, vol. 7, pp. 33–43.
28. D.P. Lorento: *Billet Mold Taper and Secondary Cooling Pattern Design*, Private Communication, 2002.
29. B.G. Thomas and C. Ojeda: in *ISS Steelmaking Conference*, ISS-AIME, Indianapolis, IN, 2003, pp. 295–308.
30. C. Li and B.G. Thomas: in *85th Steelmaking Conference Proceedings*, Iron and Steel Society, Warrendale, PA, 2002, pp. 109–30.
31. C. Li and B.G. Thomas: in *ISS Steelmaking Conference*, ISS-AIME, Indianapolis, IN, 2003, pp. 685–700.
32. M.R. Ridolfi, B.G. Thomas, G. Li, and U. Della Foglia: *La Rev. Metall.*, 1994, vol. 91, pp. 609–20.
33. B.G. Thomas and W.R. Storkman: in *Modeling Control of Casting and Welding Processes - IV*, A.F. Giamei and G.J. Abbaschian, eds., The Metallurgical Society, Palm Coast, FL, 1988, pp. 287–97.
34. A. Moitra, B.G. Thomas, and W.R. Storkman: in *TMS Annual Meeting*, The Minerals, Metals & Materials Society, San Diego, CA, 1992, pp. 1–31.
35. M. Bellet, O. Jaouen, and I. Poitrault: *Int. J. Numer. Methods Heat Fluid Flow*, 2005, vol. 15, pp. 120–42.
36. M. Bellet and V.D. Fachinotti: in *Modeling Casting Welding Advanced Solidification Processes. IX*, C.A. Gandin and M. Bellet, eds., The Minerals, Metals & Materials Society, Opio, France, 2006, pp. 169–76.
37. B. Bottger, M. Apel, M.B. Santillana, and D. Eskin: *Metall. Mater. Trans. A*, 2013, vol. 44A, pp. 3765–77.
38. J. Tiaden: *J. Cryst. Growth*, 1999, vols. 198–199, pp. 1275–80.
39. B. Bottger, G.J. Schmitz, and M.B. Santillana: *Trans. Indian Inst. Met.*, 2012, vol. 65, pp. 613–15.
40. B.G. Thomas and J.T. Parkman: in *Materials Society Annual Meeting*, M. Chu and E. Lavernia, eds., The Minerals, Metals & Materials Society, San Antonio, TX, 1998, pp. 509–20.
41. J.K. Brimacombe: *Can. Metall. Q.*, 1976, vol. 15, pp. 163–75.
42. C. Cicutti, M. Valdez, T. Perez, G. DiGresia, W. Balante, and J. Petroni: in *Steelmaking Conference Proceedings*, Iron and Steel Society, Warrendale, PA, 2002, pp. 97–107.
43. N. Kapaj, M. Pavlicevic, and A. Poloni: in *Steelmaking Conference Proceedings*, Iron and Steel Society, Warrendale, PA, 2001, pp. 369–76.
44. J.K. Park, I.V. Samarasekera, B.G. Thomas, and U.S. Yoon: *Metall. Mater. Trans. B*, 2002, vol. 33B, pp. 425–36.
45. M.M. Wolf: *Iron Steelmak.*, 1996, vol. 23, pp. 47–51.

46. P. Duvvuri, B. Petrus, and B.G. Thomas: in *AISTech - Iron Steel Technology Conference Proceedings*, AIST, Indianapolis, IN, 2014, pp. 2881–94.
47. A.W. Cramb: in *Fundam. Metall.*, Elsevier, 2005, pp. 399–452.
48. M.M. Wolf: in *Continuous Casting Vol 9, Initial Solidification Strand Surface Quality of Peritectic Steels*, M.M. Wolf, ed., Iron and Steel Society/AIME, Warrendale, PA, 1997, pp. 211–29.
49. J. Konishi, M. Militzer, I.V. Samarasekera, and J.K. Brimacombe: *Metall. Mater. Trans. B*, 2002, vol. 33B, pp. 413–23.
50. S. Koric, L.C. Hibbeler, R. Liu, and B.G. Thomas: *Numer. Heat Transf. Part B Fundam.*, 2010, vol. 58, pp. 371–92.
51. B.G. Thomas, R. O'Malley, T. Shi, Y. Meng, D. Creech, and D. Stone: in *Modeling Casting Welding Advanced Solidification Processes IX*, 2000, pp. 769–76.
52. S. Koric and B.G. Thomas: *J. Mater. Process. Technol.*, 2008, vol. 197, pp. 408–18.
53. S. Koric and B.G. Thomas: *Int. J. Numer. Methods Eng.*, 2006, vol. 66, pp. 1955–89.
54. Y.M. Won, K.H. Kim, T.J. Yeo, and K.H. Oh: *ISIJ Int.*, 1998, vol. 38, pp. 1093–99.
55. R.D. Cook: *Concepts and Applications of Finite Element Analysis*, Wiley, 1989.
56. ABAQUS: *ABAQUS 6.13 Theory Manual*, DS SIMULIA Corp, Providence, RI, 2013.
57. ABAQUS: *ABAQUS 6.13 Subroutine Manual*, DS SIMULIA Corp, Providence, RI, 2013.
58. L.C. Hibbeler and B.G. Thomas: in *6th European Continuous Casting Conference*, Association Italiana Metallurgia, Ricionne, Italy, 2008, pp. 1–16.
59. Y. Meng and B.G. Thomas: *Metall. Mater. Trans. B*, 2003, vol. 34B, pp. 685–705.
60. Y.M. Won and B.G. Thomas: *Metall. Mater. Trans. A*, 2001, vol. 32A, pp. 1755–67.
61. K. Harste: Ph.D. Thesis, Technischen Universität Clausthal, 1989.
62. K. Harste and K. Schwerdtfeger: *ISIJ Int.*, 2003, vol. 43, pp. 1011–20.
63. I. Jimbo and A.W. Cramb: *Metall. Mater. Trans. B*, 1993, vol. 24B, pp. 5–10.
64. H. Mizukami, A. Yamanaka, and T. Watanabe: *ISIJ Int.*, 2002, vol. 42, pp. 375–84.
65. B.G. Thomas, I.V. Samarasekera, and J.K. Brimacombe: *Metall. Mater. Trans. B*, 1987, vol. 18B, pp. 131–47.
66. J. Lubliner: *Plasticity Theory*, Revised, 2005.
67. H. Zhu: Ph.D. Thesis, The University of Illinois at Urbana-Champaign, 1996.
68. P.F. Kozlowski, B.G. Thomas, J.A. Azzi, and H. Wang: *Metall. Mater. Trans. A*, 1992, vol. 23A, pp. 903–18.
69. D. Slavik and H. Sehitoglu: *J. Eng. Mater. Technol.*, 1986, vol. 108, pp. 303–12.
70. J.H. Weiner and B.A. Boley: *J. Mech. Phys. Solids*, 1963, vol. 1, pp. 145–54.
71. M. Rowan, B.G. Thomas, R. Pierer, and C. Bernhard: *Metall. Mater. Trans. B*, 2011, vol. 42B, pp. 837–51.
72. M.L.S. Zappulla: Master's Thesis, The University of Illinois at Urbana-Champaign, 2016.
73. R. Pierer, C. Bernhard, and C. Chimani: *La Rev. Metall.*, 2007, vol. 3, pp. 72–83.
74. B.G. Thomas, A. Moitra, and R. McDavid: *Iron Steelmaker (ISS Trans.)* 1996, vol. 23, pp. 143–56.
75. T. Murakami and H. Kashima-cho: in *Current Advanced Materials Processes Report ISIJ Meeting*, Iron and Steel Institute of Japan, Tokyo, 1992, p. 1291.
76. L.C. Hibbeler, B.G. Thomas, R.C. Schimmel, and G. Abbel: *Metall. Mater. Trans. B*, 2012, vol. 43B, pp. 1156–72.
77. Y.M. Won, T.J. Yeo, K.H. Oh, J.K. Park, J. Choi, and C.H. Yim: *ISIJ Int.*, 1998, vol. 38, pp. 53–62.